Simplified model for unsteady air cavities under ship hulls

Konstantin I. Matveev

Washington State University, Pullman, WA, USA

Abstract

The drag reduction technique involving air cavities under ship hulls is a promising energy-saving technology. Understanding the air cavity dynamics in unsteady conditions and developing methods for the air cavity system optimization are critically important for practical implementation of this technology. In this study, a potential flow theory is applied for modeling the air cavities under solid walls in water flow with fluctuating pressure. The present modeling approach incorporates detachment of macroscopic air pockets from the cavity tail. For specific configurations considered in this paper, it is found that a change of the rate of air supply into the cavity can partly mitigate degradation of the overall power savings by the air cavity system in unsteady conditions.

Keywords: Ship drag reduction; air cavity system; numerical modeling; potential flow theory.

Introduction

Reducing environmental impact and improving sustainability of marine transportation are important contemporary tasks of maritime engineering. These goals can be addressed by developing novel technologies that reduce hydrodynamic resistance of ships hulls and thus decrease fuel consumption and emissions. One promising approach is to employ air cavities under ship hulls that separate a significant fraction of the hull surface from contact with water and hence lead to lower frictional drag. Two examples of the air-cavity systems under ship hulls are illustrated in Fig. 1. Although this idea has been known and studied for a long time and even implemented on a handful of ships and boats [1,2], its broad implementation has not occurred, especially for seagoing vessels, due to lack of understanding how to design robust air-cavity systems that can usefully operate in variable conditions.

The seemingly simple idea of supplying air to the wetted hull surfaces with a purpose to reduce drag involves rather complex multi-phase/surface turbulent flows with important roles of gravity, restrictive solid boundaries (ship hulls), and other physical phenomena [3]. A large body of basic knowledge on air-cavity flows under solid walls has been accumulated in the last two decades, and a number of model-

scale studies have been conducted, primarily in steady environments [4-8]. However, several investigations also included variations of external conditions [9-13].

The development of ocean-going ships with air cavities requires analysis of the air cavity behavior in unsteady environments that can assist with the design of more robust systems. Moreover, it is likely that some sort of active control will be needed for air-cavity systems on ocean-going vessels. Effects of hydrodynamic elements (imitating interceptors and propulsors) on steady properties of an air cavity were previously analyzed [14]. It was experimentally shown that a hydrofoil located under a cavity can increase a length of a stable cavity and therefore enhance its drag-reducing capability [15]. With advanced computational techniques, the unsteady behavior of an air cavity, corresponding to a laboratory setup described in [10], was modeled in [16]. Effects of air supply rates on economics of drag reduction systems were considered in [17]. Some results for flow control involving active cavitators (solid parts where the air cavity is initiated) were recently presented in [18].

The main goals of this paper are to introduce a simplified numerical model for an unsteady air cavity, simulate air cavity dynamics in time-dependent external conditions, and demonstrate how variable air supply can mitigate deterioration of the air-cavity drag reduction ability. This model can assist marine engineers in preliminary estimations of the air-cavity system performance and can be used for guiding more elaborate experimental or computational fluid dynamics (CFD) studies. Details of the technical implementation of the air-cavity system, such as selection of the air pumping components and structural aspects of hulls with modified bottom geometry to accommodate air cavities, are beyond the scope of the present study.

A hydrodynamic part of the present model, which employs a potential-flow theory, has been previously applied and validated for several related problems, including planing hulls [19,20], air-cavity and air-cushion setups [4,21], and supercavitating flow [15].

Mathematical Model

A two-dimensional problem schematic with a backward-facing step is shown in Fig. 2a. The water flow is assumed incompressible, irrotational and inviscid. Far upstream of the step the flow is uniform. A cavity filled with compressible air is present behind the step. The air is assumed uniform with the same pressure and density throughout the cavity, although these properties, as well as the cavity shape, may

change in time. The air velocities are neglected, and the air density is much smaller than the water density. On the water streamline at the cavity boundary both the dynamic and kinematic boundary conditions for the water flow must be satisfied. The dynamic condition can be described by the unsteady Bernoulli equation [22],

$$p_w + \frac{1}{2}\rho_w U^2 = p_c + \frac{1}{2}\rho_w u^2 + \rho_w g y_w + \rho_w \frac{\partial \varphi\prime}{\partial t}, \quad (1)$$

where p_w is the upstream water pressure at y = 0 (at the wall in front of the step), ρ_w is the water density, U is the velocity in the incident flow, p_c is the pressure inside the air cavity, u is the water velocity on the cavity boundary, g is the gravitational constant, y_w is the vertical coordinate of the cavity boundary, and φ' is the perturbation component of the water velocity potential.

Only a linear formulation is considered in this analysis that implies small water surface slopes and small perturbation velocities. Then, linearized Eq. (1) can be written in a non-dimensional form,

$$\widetilde{u'} + \frac{\tilde{y}_w}{Fr_H^2 \widetilde{H}} + \frac{\partial \widetilde{\varphi}}{\partial \tilde{t}} = \frac{\sigma}{2}, \quad (2)$$

where $\widetilde{u'} = (u_x - U)/U$ is the normalized horizontal velocity perturbation on the cavity surface, $\tilde{y}_w = y_w/L$ and $\widetilde{H} = H/L$ are the non-dimensional ordinates of the cavity boundary and the step height, respectively, L is the computational domain length selected here to be longer than the air cavity (Fig. 2a), $Fr_H = U/\sqrt{gH}$ is Froude number based on the step height , $\widetilde{\varphi'} = \varphi'/(UL)$ is the normalized perturbation potential, and $\tilde{t} = tU/L$ is the non-dimensional time. The term on the right-hand side of Eq. (2) is the cavitation number,

$$\sigma = \frac{p_w - p_c}{0.5\rho_w U^2}. \quad (3)$$

A linear form of the kinematic boundary condition relates the surface elevation to the perturbed velocity potential [22],

$$\frac{\partial \varphi\prime}{\partial y} = U\frac{\partial y_w}{\partial x} + \frac{\partial y_w}{\partial t}, \quad (4)$$

which non-dimensional counterpart can be written as follows,

$$\frac{\partial \widetilde{\varphi\prime}}{\partial \tilde{y}} = \frac{\partial \widetilde{y_w}}{\partial \tilde{x}} + \frac{\partial \widetilde{y_w}}{\partial \tilde{t}}. \quad (5)$$

In the present model, potential hydrodynamic sources placed on the water boundary are employed in order to find a solution. In this approach, the vertical water velocity v represented by the left-hand side term in Eq. (4) can be related to the local source density q [23],

$$\frac{\partial \varphi\prime}{\partial y} = v = -\frac{q}{2}. \quad (6)$$

The sign minus in Eq. (5) indicates that positive sources distributed along the wall will generate downward velocity in the water flow. Furthermore, the current method employs discrete (point) sources (Fig. 2b), while the collocation points, where the boundary conditions are imposed, are shifted upstream from the sources to minimize the effect of the downstream boundary [24]. Hence, a discretized form of Eq. (6) can be expressed as follows,

$$\frac{\partial \tilde{\varphi}'}{\partial \tilde{y}}(\tilde{x}_i^c) \approx -\frac{\tilde{Q}_i+\tilde{Q}_{i-1}}{4\Delta\tilde{x}}, \quad (7)$$

where x_i^c is the position of the i-th collocation point, Q_i and Q_{i-1} are intensities of the neighboring point sources, and Δx is the distance between neighboring sources (or collocation points). The total number of sources (or collocation points) is N.

The normalized horizontal velocity perturbation and its potential at each collocation point can be related to intensities of all sources, which are distributed in the computational domain between $x = 0$ and $x = L$, using standard expressions from the two-dimensional potential theory,

$$\tilde{\varphi}(\tilde{x}_i^c) = \frac{1}{2\pi}\sum_j \tilde{Q}_j \ln\left|\tilde{x}_i^c - \tilde{x}_j^s\right|, \quad (8)$$

$$\widetilde{u'}(\tilde{x}_i^c) = \frac{1}{2\pi}\sum_j \frac{\tilde{Q}_j}{\tilde{x}_i^c - \tilde{x}_j^s}, \quad (9)$$

where $x_i^s = x_i^c + \Delta x/2$ are the source coordinates. The elevations of the sources and collocation points are neglected in Eqs. (8-9) due to an assumption of small water elevations and step height.

Upon substituting Eqs. (7-9) into (2) and (5) and using a first-order stepping in time, a system of $2N$ discretized equations can be written as follows,

$$\frac{1}{2\pi}\sum_j \frac{\tilde{Q}_j}{\tilde{x}_i^c - \tilde{x}_j^s} + \frac{\tilde{y}_i^s+\tilde{y}_{i-1}^s}{2Fr_H^2\tilde{H}} + \frac{1}{2\pi}\sum_j \frac{\tilde{Q}_j-\tilde{Q}_j^p}{\Delta\tilde{t}} \ln\left|\tilde{x}_i^c - \tilde{x}_j^s\right| = \frac{\sigma}{2}, \quad (10)$$

$$-\frac{\tilde{Q}_i+\tilde{Q}_{i-1}}{4\Delta\tilde{x}} = \frac{\tilde{y}_i^s-\tilde{y}_{i-1}^s}{\Delta\tilde{x}} + \frac{\tilde{y}_i^s+\tilde{y}_{i-1}^s}{2\Delta\tilde{t}} - \frac{\tilde{y}_i^p+\tilde{y}_{i-1}^p}{2\Delta\tilde{t}}, \quad (11)$$

where $\tilde{Q}_i^p$ and $\tilde{y}_i^p$ are the normalized source intensity and elevation at the previous time, and $\Delta\tilde{t} = \Delta t U/L$ is the non-dimensional time step. In case of the first collocation point ($i = 1$), one can take the upstream elevation and source intensity as zeros ($\tilde{y}_{-1}^s = 0$ and $\tilde{Q}_{-1} = 0$), since it is located on a horizontal wall at zero elevation. The unknowns in Eqs. (10-11) include $2N + 1$ variables: free surface elevations at source locations $\tilde{y}_i^s$, source intensities $\tilde{Q}_i$ (i varies from 1 to N), and a cavitation number σ. The upstream water pressure p_w and velocity U are specified in the present analysis, so cavitation number σ is essentially related to the cavity pressure. It is determined here form the mass balance

assuming an adiabatic process for air in the cavity. First, the air pressure and density are coupled to their given initial equilibrium values,

$$\frac{p_c(t)}{\rho_a^{\gamma}(t)} = const = \frac{p_c(0)}{\rho_a^{\gamma}(0)}, \quad (12)$$

where $\gamma = 1.4$ is the ratio of specific heats for air. Then, the air density can be found from the mass balance,

$$\frac{d}{dt}(m_c) = \dot{m}_{in} - \dot{m}_{out}\,, \quad (13)$$

$$m_c = \rho_a V_c\,, \quad (14)$$

where $V_c = \sum_i (H - y_i^s)\Delta x$ is the cavity volume and m_c is the mass of air in the cavity. As explained below, it is always ensured that the cavity boundary does not cross the solid wall behind the step, i.e., $y_i^s \le H$.

The input mass flow rate of air $\dot{m}_{in}$ depends on the air supply system that can be controlled. The associated compressor power P_S can be estimated as follows [25],

$$P_S = \frac{\dot{m}_{in}}{\eta_C}\frac{p_{atm}}{\rho_{atm}}\frac{\gamma}{\gamma-1}\left[\left(\frac{p_c}{p_{atm}}\right)^{\frac{\gamma-1}{\gamma}} - 1\right], \quad (15)$$

where η_C is the isentropic efficiency of the air supply system, p_{atm} and ρ_{atm} are the atmospheric pressure and density, respectively, and γ is the ratio of specific heats (γ = 1.4 for air).

The air removal rate $\dot{m}_{out}$ will be determined here considering two basic forms of air leakage from cavities under ship hulls. The first is associated with small air bubbles departing from the sides of the cavity even in steady ship sailing (Fig. 3a). This is a complex three-dimensional process beyond the present 2D analysis. In the steady case, $\dot{m}_{out,st} = \dot{m}_{in,st}$ and the input flow is approximated through a simple correlation [3],

$$\dot{m}_{out,st} = \dot{m}_{in,st} = c_Q \rho_a HWU, \quad (16)$$

where c_Q is the flow rate coefficient (with values around 0.01-0.02) and W is the cavity width. Equation (16) is in approximate agreement with other empirical correlations [17,26]. In unsteady situations, the air leakage through small bubbles shed from the cavity sides can be estimated with a modified expression. Considering relatively small deviations of the long cavity from its equilibrium state, the simplest form for the air leakage rate can be related to its current length,

$$\dot{m}_{out}(t) = \dot{m}_{out,st}\frac{L_c(t)}{L_{c0}}\,. \quad (17)$$

where L_{c0} is the equilibrium length of the air cavity. Equation (17) implies that the air leakage increases with the cavity lengthening and decreases when it becomes shorter, so the cavity tends to return to the equilibrium at a steady rate of air supply. It should be kept in mind that Eq. (17) is not valid for large fluctuations of the cavity. For example, it usually takes a large air supply rate to establish a stable long cavity from a very short cavity or from the no-cavity state. Such a flow rate can be several times bigger than that needed to maintain a stable developed cavity [9,10].

The second mechanism of air leakage considered here is associated with detachment of macroscopic air pockets from the cavity that can be caused by variation of external conditions. This process is modeled with the two-dimensional theory outlined above. The air cavity can start growing when, for example, the air supply is intentionally increased or the water pressure drops in the incident flow. In such cases, the cavity will elongate (Fig. 3b), and its surface may approach and touch the hard ceiling (Fig. 3c). In the present approach, similar to modeling in [16], it is assumed that upon the cavity reaching the wall the downstream part of the air cavity is shed away. However, in the current analysis it is also assumed that the detached pocket no longer influences the air remaining in the upstream part of the cavity. In the present numerical implementation, the source elevations are checked whether they reached or exceeded the step height. If this happens for the i-th source, i.e., $y_i^s > H$, then the source elevations downstream are forced to be at the step position, $y_j^s = H$ for $j \geq i$. The downstream source intensities are made zero, $Q_j = 0$ for $j > i$, and the i-th source's strength is determined from Eq. (11) using information about the surface vertical velocity. During this detachment event, the air cavity volume and mass undergo step jumps, decreasing by the following amounts,

$$\Delta V_c = \sum_{j \geq i} (H - y_j^s) \Delta x \,, \tag{18}$$

$$\Delta m_c = \rho_a \Delta V_c. \tag{19}$$

Then, the air-cavity mass change (Eq. 13) during one time step can be re-written in the discretized form as follows,

$$m_c - m_c^p = \dot{m}_{in} \Delta t - \dot{m}_{out} \Delta t - \Delta m_c \,, \tag{20}$$

where m_c^p is the mass of air in the cavity at the previous time and Δm_c is non-zero only at time moments when the cavity surface reaches the wall at a location upstream of the cavity tail. This mass balance equation together with Eq. (14), which relates the air cavity mass to the cavity volume and the air density, is used to update a cavitation number in Eq. (10). For the calculation examples shown below, it was established that the number of sources $N = 100$ achieves adequate mesh independency and the non-dimensional time step $\Delta \tilde{t} = 0.5 \Delta x / L$ ensures numerical stability.

To evaluate net power savings achieved with application of air cavities, one can compare the air supply system power with a reduction of the propulsion system power P_D due to reduced wetted area of the ship hull. This reduction is estimated here with effective friction coefficient C_f and propulsion system efficiency η_P,

$$P_D = \frac{C_f}{\eta_P}\frac{\rho_w U^3}{2} A_c \,, \qquad (21)$$

where $A_c = L_c W$ is the area covered by the air cavity.

Results

An illustration of a validation example of the present mathematical model for a steady air cavity is given in Fig. 4. A model-scale two-dimensional hull was tested previously in a water channel [4]. An air cavity was produced by supplying air behind a step on the hull bottom (Fig. 4a). Test data for lengths of stable air cavities obtained with small air supply rates are compared in Fig. 4b against numerical predictions by the potential-flow theory at various flow speeds and two hull submergences. A good agreement demonstrates an ability of the linearized potential-flow model to adequately predict shapes of elongated air cavities under solid surfaces.

Another validation case is shown in Fig. 5a for unsteady water surface deformations due to oscillating pressure patch moving above and parallel to the water surface. This problem was analyzed analytically in [27] The non-dimensional in-phase and out-of-phase water surface elevations $y_1 = y_w \rho_w g / p_1$ behind the patch with sinusoidal pressure fluctuations of magnitude p_1 are given in Fig. 5b,c. These results are obtained for a specific condition with a patch length Froude number $Fr_c = U/\sqrt{gc}$ = 1.3 and a non-dimensional frequency of pressure oscillations $4\omega U/g$ = 5. The agreement between the theoretical solution and the numerical results is good, indicating an ability of the current model to adequately handle unsteady surface flows.

To demonstrate the process of air pocket detachment from the air cavity behind a step (Fig. 2) simulated with the present method, the air cavity response to a sudden change of the pressure in the water flow has been modeled assuming constant flow rate of air supplied into the cavity. The cavity starts from an equilibrium state (when air inflow is equal to air leakage) with realistic operational characteristics: incident water speed U = 6 m/s, step height H = 0.1 m, and step submergence 5 m. The step height

Froude number is therefore $Fr_H = U/\sqrt{gH} \approx 6$. The flow rate leakage coefficient in Eq. (16) is chosen as c_Q = 0.015. The equilibrium air-cavity pressure is assumed equal to the hydrostatic pressure at the mid-plane between upstream and downstream walls, which corresponds to the cavitation number σ = 0.0278. The steady-state two-dimensional air-cavity characteristics (length, volume, air mass, and pressure) are shown in Fig. 6 at time zero. The equilibrium cavity shape is given in Fig. 7a with the cavity length of about 8 m.

At time t = 0.02 s, the pressure in the water flow is prescribed to suddenly drop by about 6.6% (Fig. 6d). This causes the cavity expansion (Fig. 6a,b) and formation of waves on the cavity surface near the step and the cavity tail (Fig. 7b). The cavity pressure starts dropping as well (Fig. 6d). Since the air cavity elongates, the air leakage through small bubbles slightly increases, according to Eq. (17), which results in gradual reduction of the air cavity mass (Fig. 6c). Due to air compressibility, the cavity volume and pressure also undergo oscillations noticeable in Fig. 6b,d. The wave at the cavity tail propagates further downstream creating a pocket susceptible to shedding from the cavity (Fig. 7c). When the crest of the water surface touches the ceiling, the pocket detaches. At this instant (happening around 0.45 s) the air cavity losses mass (Fig. 6c) and its length and volume contract (Fig. 6a,b). The cavity shape after the pocket detachment is shown in Fig. 7d. This process repeats several times until sufficient mass of air is lost. Then, the cavity continues to oscillate, and eventually it settles at a new equilibrium state corresponding to reduced pressure in the water flow.

Another modeling example is presented here for oscillatory variation of the water pressure that can partially simulate heaving motions of a hull neglecting changes in the incident flow velocity and three-dimensional effects. It is assumed that the water pressure varies as follows,

$$p_w(t) = p_{w0} + p_{w1}\sin(2\pi f t), \qquad (22)$$

where p_{w0} is the steady component, corresponding to the equilibrium state, p_{w1} is the amplitude of pressure fluctuation, and f is the frequency. Two amplitudes are chosen here, p_{w1}/p_{w0} equal to 0.033 and 0.1, while the frequency is taken as 0.15 Hz. Since the unsteady conditions are likely to result in higher air leakage, the drag reduction performance of the air cavity is expected to degrade. One can try to partly mitigate this effect by adjusting the air supply rate. In this study several constant values of supply rate of air were modeled around the value corresponding to the steady equilibrium condition. The ratio of mass flow rates $k_m = \dot{m}_{in}/\dot{m}_{in,0}$ was varied between 0.9 and 1.1. The cavity parameters and incident flow velocity are the same as in the previous example, whereas it is assumed that cavity

width is 10 m in order to obtain numerical values of interest to practical situations. The initial conditions correspond to the steady equilibrium state.

The time variations of pressure in the incident water flow, as well as mass of air in the cavity and the cavity volume, are shown in Fig. 8 for two magnitudes of pressure fluctuations and the equilibrium air supply rate $\dot{m}_{in,0}$. The pressure varies sinusoidally (Fig. 8a) in accordance with Eq. (22). In the first cycle during the phase of pressure decrease, the air cavity increases, and some air departs from the cavity via several detached pockets similar to the process described above. As a consequence, the mass of the air in the cavity decreases, and its time-averaged value approaches a constant (Fig. 8b). The resulting mass loss is larger for higher amplitude pressure fluctuations. The cavity volume exhibits oscillatory motions (Fig. 8c) similar to the previously considered case (Fig. 6d), and the mean volume value also decreases. Therefore, it can be expected the drag reducing capability of the air cavity will degrade such unsteady conditions.

The net power savings due to air cavity constitute the difference between reduction of propulsion system power because of reduced drag (Eq. 21) and the power of the air supply system (Eq. 15). For power calculations, it is assumed that the friction coefficient is $C_f = 0.004$, the overall efficiency of the propulsion system is $\eta_P = 0.65$, and the overall efficiency of the air supply system is $\eta_S = 0.45$. The net power saving metric $P_D - P_S$ is shown in Fig. 9 for the case of no fluctuations in the water flow pressure, as well as for two amplitudes of pressure variations. The power savings degrade with increase of the oscillation magnitude. For example, at the constant (equilibrium) air flow rate the savings drop from about 41 kW down to 39.5 kW and 36 kW at two considered levels of fluctuations.

One can attempt to reduce this degradation of performance by adjusting the air supply rate. The calculations with the present setup indicate that it is beneficial to raise the supply rate by 5% at the condition when p_{w1}/p_{w0} = 0.033 (Fig. 9b). While more power is need to increase the air supply, longer cavity can be maintained, and the overall effect will optimize the system performance. Further increase of air flow is not beneficial since more air will be lost through detaching air pockets. Reducing flow rate at this condition will result in shorter cavities with larger performance degradation.

In contrast, at higher amplitudes of pressure fluctuations in the water flow, the slight improvement can be achieved by decreasing the air supply rate (Fig. 9c). The unsteadiness in the water flow is greater in

this case, and maintaining long air cavities is problematic, since the air is more easily shed away. It appears that decrease of air inflow by 5% would allow saving more power in the air supply system than the increased amount of propulsion power.

It should be noted that the presented calculation results are specific to the studied conditions and subject to the several assumptions, such as two-dimensional flow under infinite walls. Hence, these results should be treated only as examples of possible performance trends of the air-cavity systems.

Conclusions

A simplified potential-flow method has been developed for unsteady modeling of air cavities formed under horizontal walls, including processes of air pocket detachment. The model application for a situation with oscillatory pressure in the flow demonstrated degradation of the air-cavity drag reduction due to air loss from the cavity and a subsequent cavity contraction. Manipulation of the air supply rate can partly alleviate decrease of power savings in unsteady conditions. For specific setups considered in this study it is found that an increase of the air supply is beneficial at low amplitudes of pressure fluctuations in the flow, whereas a slight decrease of air supply provides more optimal operational state with regard to the overall power savings at high amplitudes of pressure oscillations.

Promising directions for future model developments include three-dimensional and more complex geometrical configurations, nonlinear formulation, addition of surface tension, and incorporation of moving solid parts, such as morphing hull surface, which can lead to higher performance of air-cavity drag reduction systems in broader range of operational conditions. Additional validation studies against well-defined experiments with high spatio-temporal resolution of air-cavity flows will be of great value as well.

Acknowledgement

This material is based upon research supported by the National Science Foundation under Grant No. 1800135.

References

1. Latorre R. Ship hull drag reduction using bottom air injection. *Ocean Engineering* 1997; 24: 161-175.
2. Matveev KI. Application of artificial cavitation for reducing ship drag. *Oceanic Engineering International* 2005; 9(1): 35-41.
3. Ceccio SL. Friction drag reduction of external flows with bubble and gas injection. *Annual Review of Fluid Mechanics* 2010; 42: 183-203.
4. Matveev KI, Burnett T and Ockfen A. Study of air-ventilated cavity under model hull on water surface. *Ocean Engineering* 2009; 36(12-13): 930-940.
5. Lay KA, Yakushiji R, Makiharju S, Perlin M and Ceccio SL. Partial cavity drag reduction at high Reynolds numbers. *Journal of Ship Research* 2010; 54: 109-119.
6. Makiharju SA, Elbing BR, Wiggings A, Shinasi S, Vanden-Broeck J-M, Perlin M, Dowling DR and Ceccio SL. On the scaling of air entrainment from a ventilated partial cavity. *Journal of Fluid Mechanics* 2013; 732: 47-76.
7. Shiri A, Leer-Andersen M, Bensow RE and Norrby J. Hydrodynamics of a displacement air cavity ship. In: *29th Symposium on Naval Hydrodynamics*, Gothenburg, Sweden, 2012.
8. De Marco A, Mancini S, Miranda S, Scognamiglio R and Vitiello L. Experimental and numerical analysis of a stepped planing hull. *Applied Ocean Research* 2017; 64: 135-154.
9. Arndt REA, Hambleton WT, Kawakami E and Amromin EL. Creation and maintenance of cavities under horizontal surfaces in steady and gust flows. *Journal of Fluids Engineering* 2009; 131: 111301-1.
10. Makiharju SA, Elbing BR, Wiggings A, Dowling DR, Perlin M and Ceccio SL. Perturbed partial cavity drag reduction at high Reynolds numbers. In: *28th Symposium on Naval Hydrodynamics*, Pasadena, California, USA, 2009.
11. Amromin E, Karafiath G and Metcalf B. Ship drag reduction by air bottom ventilated cavitation in calm water and in waves. *Journal of Ship Research* 2011: 55: 196-207.
12. Zverkhovskyi O, Van Terwisga T, Gunsing M, Westerweel J and Delfos R. Experimental study on drag reduction by air cavities on a ship model. In: *30th Symposium on Naval Hydrodynamics*, Hobart, Tasmania, Australia, 2014.
13. Butterworth J, Atlar M and Shi W. Experimental analysis of an air cavity concept applied on a ship hull to improve the hull resistance. *Ocean Engineering* 2015; 110: 2-10.
14. Matveev KI. On the limiting parameters of artificial cavitation. *Ocean Engineering* 2003; 30(9): 1179-1190.

15. Matveev KI and Miller MJ. Air cavity with variable length under model hull. *Journal of Engineering for the Maritime Environment* 2011; 225(2): 161-169.
16. Choi J-K and Chahine L. Numerical study on the behavior of air layers used for drag reduction. In: *28th Symposium on Naval Hydrodynamics*, Pasadena, California, USA, 2010.
17. Makiharju SA, Perlin M and Ceccio SL. On the energy economics of air lubrication drag reduction. *International Journal of Naval Architecture and Ocean Engineering* 2012; 4: 412-422.
18. Amromin E. Ships with ventilated cavitation in seaways and active flow control. *Applied Ocean Research* 2015; 50: 163-172.
19. Matveev KI and Ockfen A. Modeling of hard-chine hulls in transitional and early planing regimes by hydrodynamic point sources. *International Shipbuilding Progress* 2009; 56(1-2): 1-13.
20. Matveev KI. Hydrodynamic modeling of planing hulls with twist and negative deadrise. *Ocean Engineering* 2014; 82: 14-19.
21. Matveev KI and Chaney C. Heaving motions of a ram wing translating above water. *Journal of Fluids and Structures* 2013; 38: 164-173.
22. Newman JN. *Marine Hydrodynamics*. Cambridge, MA, USA: MIT Press, 1977.
23. Katz J and Plotkin A. *Low-Speed Aerodynamics*. Cambridge, UK: Cambridge University Press, 2001.
24. Bertram V. *Practical Ship Hydrodynamics*. Oxford, UK: Butterworth-Heinemann, 2000.
25. Cengel YA and Boles MA. *Thermodynamics: An Engineering Approach*. New York, USA: McGraw-Hill, 2015.
26. Amromin E. Analysis of interaction between ship bottom air cavity and boundary layer. *Applied Ocean Research* 2016; 59: 451-458.
27. Magnuson H. The disturbance produced by an oscillatory pressure distribution in uniform translation on the surface of a liquid. *Journal of Engineering Mathematics* 1977; 11: 121-137.

Figure captions

Fig. 1 Examples of possible implementations of air-cavity systems. (a) Single multi-wave cavity; (b) system of single-wave cavities.

Fig. 2 (a) Schematic of two-dimensional air-cavity flow around a step. (b) Horizontal positions of sources and collocation points. Step height and distances between neighboring sources are exaggerated.

Fig. 3 (a) Bottom view on the cavity illustrating air leakage through small bubbles shed at the cavity sides. (b) Side view on elongated air cavity. (c) Side view on air cavity at the moment of large air pocket detachment.

Fig. 4 (a) Schematic of tested air-cavity hull. (b) Length of air cavity. Symbols, experimental data; curves, numerical results. Solid line and circles correspond to relative draft d/H = 1.4; dashed curve and squares are for d/H = 4.3. Error bars indicate experimental uncertainties.

Fig. 5 (a) Schematic of oscillating pressure patch translating over water surface. Wave elevations: (b) in-phase and (c) out-of-phase components. Curves, current numerical results; squares, previous analytical solution.

Fig. 6 Time evolution of cavity characteristics upon step change of external pressure: (a) cavity length, (b) cavity volume per unit width, (c) mass of air in the cavity per unit width, and (d) upstream water pressure (solid line) and cavity pressure (dashed line).

Fig. 7 Cavity shapes (dashed lines) at times: (a) t = 0 s (equilibrium state), (b) t = 0.1 s, (c) t = 0.35 s, and (d) t = 0.47 s. Ready-to-detach air pocket can be noticed at the cavity tail in (c). Solid lines indicate rigid hull surfaces.

Fig. 8 Time variation of (a) upstream water pressure, (b) mass of air in the cavity, and (c) cavity volume. Solid lines, p_{w1}/p_{w0} = 0.033; dashed line, p_{w1}/p_{w0} = 0.01.

Fig. 9 Time-average net power savings at different rates of air supply and magnitudes of pressure variation. (a) p_{w1}/p_{w0} = 0, (b) p_{w1}/p_{w0} = 0.033, and (c) p_{w1}/p_{w0} = 0.1.

Figures

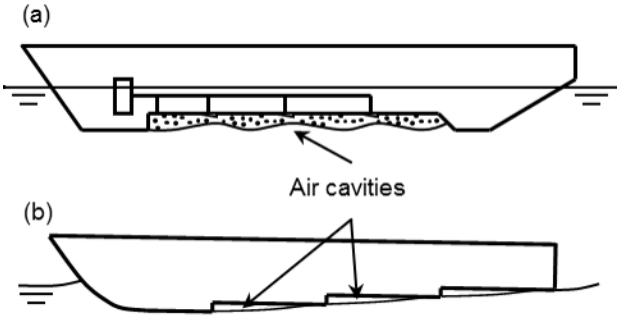

Fig. 1 Examples of possible implementations of air-cavity systems. (a) Single multi-wave cavity; (b) system of single-wave cavities.

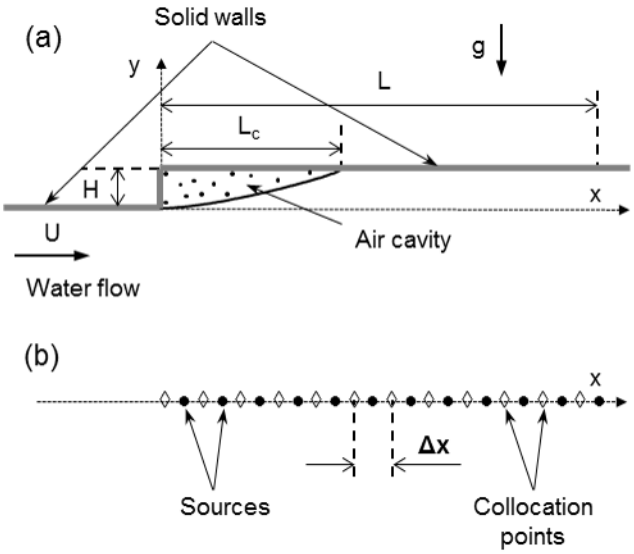

Fig. 2 (a) Schematic of two-dimensional air-cavity flow around a step. (b) Horizontal positions of sources and collocation points. Step height and distances between neighboring sources are exaggerated.

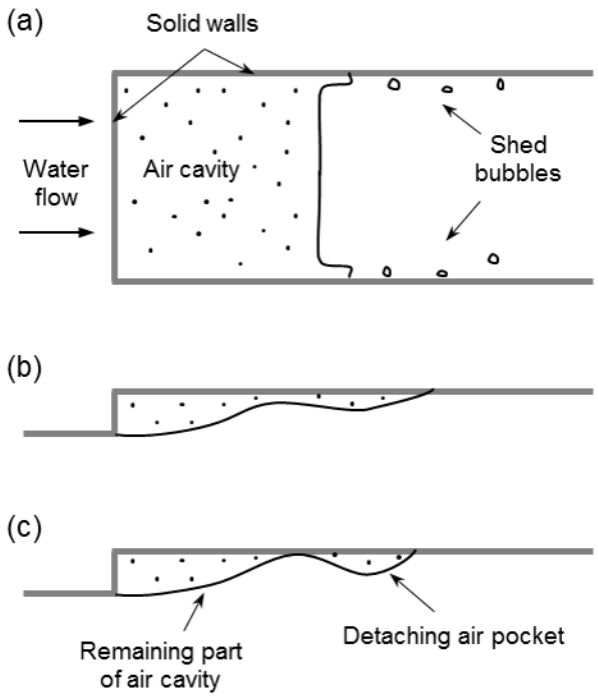

Fig. 3 (a) Bottom view on the cavity illustrating air leakage through small bubbles shed at the cavity sides. (b) Side view on elongated air cavity. (c) Side view on air cavity at the moment of large air pocket detachment.

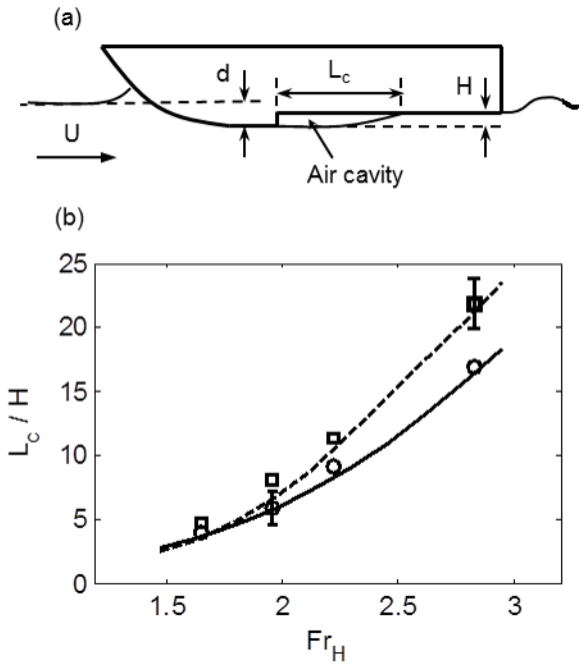

Fig. 4 (a) Schematic of tested air-cavity hull. (b) Length of air cavity. Symbols, experimental data; curves, numerical results. Solid line and circles correspond to relative draft d/H = 1.4; dashed curve and squares are for d/H = 4.3. Error bars indicate experimental uncertainties.

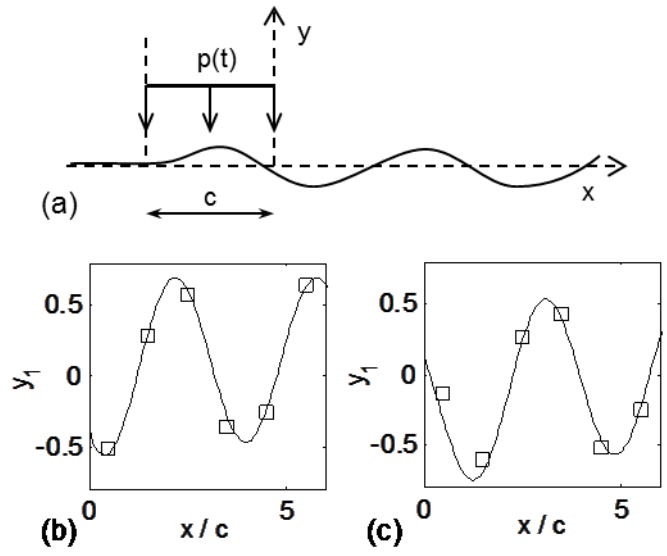

Fig. 5 (a) Schematic of oscillating pressure patch translating over water surface. Wave elevations: (b) in-phase and (c) out-of-phase components. Curves, current numerical results; squares, previous analytical solution.

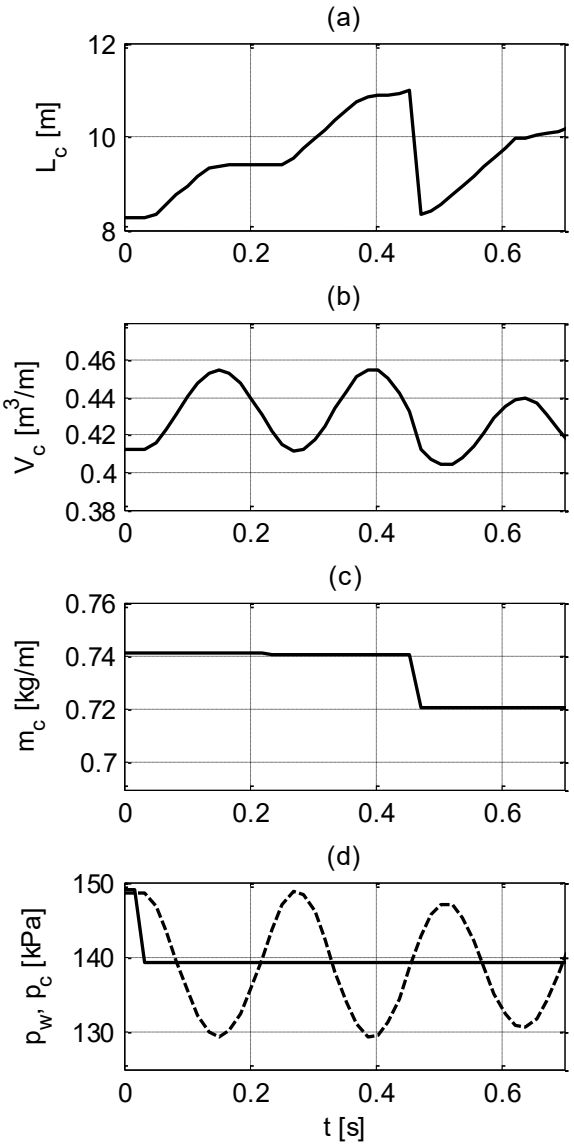

Fig. 6 Time evolution of cavity characteristics upon step change of external pressure: (a) cavity length, (b) cavity volume per unit width, (c) mass of air in the cavity per unit width, and (d) upstream water pressure (solid line) and cavity pressure (dashed line).

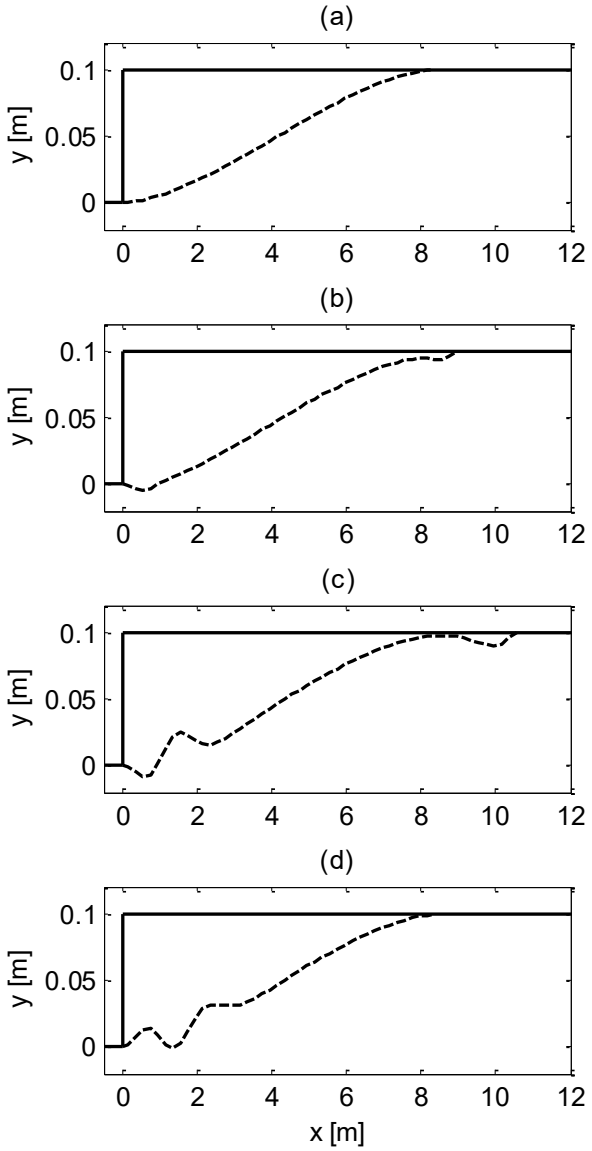

Fig. 7 Cavity shapes (dashed lines) at times: (a) t = 0 s (equilibrium state), (b) t = 0.1 s, (c) t = 0.35 s, and (d) t = 0.47 s. Ready-to-detach air pocket can be noticed at the cavity tail in (c). Solid lines indicate rigid hull surfaces.

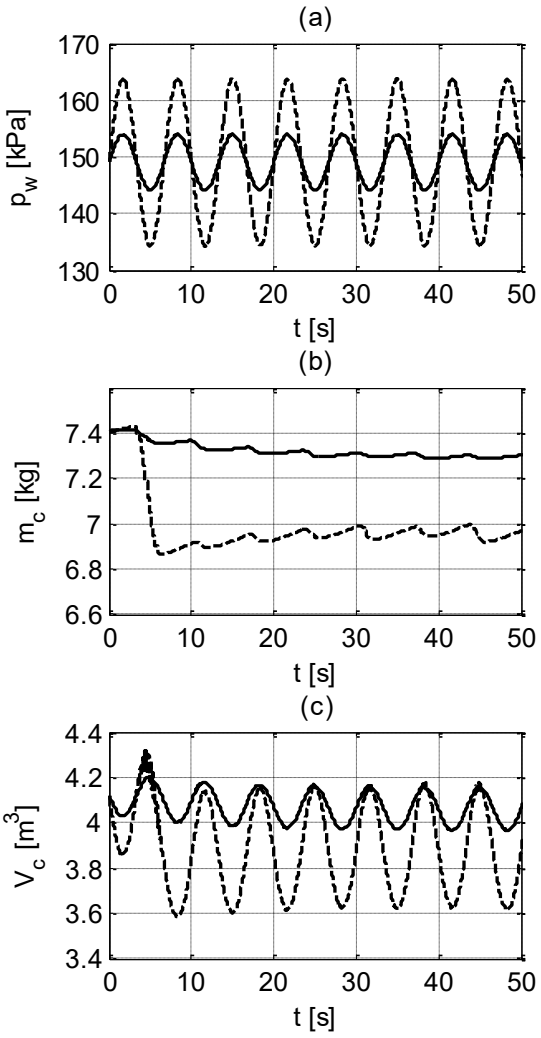

Fig. 8 Time variation of (a) upstream water pressure, (b) mass of air in the cavity, and (c) cavity volume. Solid lines, p_{w1}/p_{w0} = 0.033; dashed line, p_{w1}/p_{w0} = 0.01.

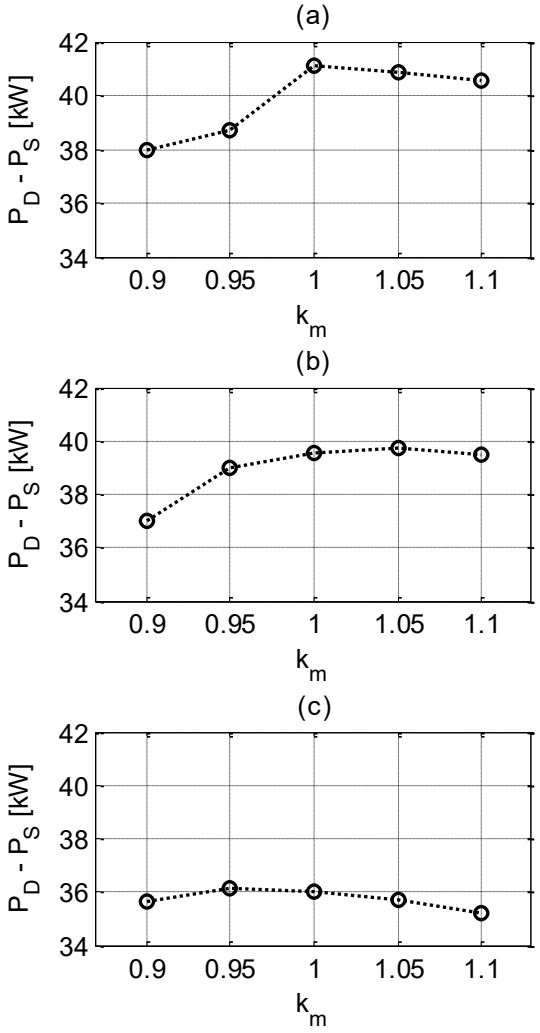

Fig. 9 Time-average net power savings at different rates of air supply and magnitudes of pressure variation. (a) p_{w1}/p_{w0} = 0, (b) p_{w1}/p_{w0} = 0.033, and (c) p_{w1}/p_{w0} = 0.1.